SELF-HEALING SYSTEM FOR HYPERVELOCITY IMPACT PROTECTION, REPAIR AND DEBRIS MITIGATION

Laura Pernigoni[(1)], Paolo Alessandro Sardelli[(1)], Ugo Lafont[(2)], Antonio Mattia Grande[(1)]

[(1)] *Department of Aerospace Science and Technology, Politecnico di Milano, via La Masa 34, 20156 Milano, Italy, Emails: laura.pernigoni@polimi.it, paoloalessandro.sardelli@mail.polimi.it, antoniomattia.grande@polimi.it*

[(2)] *ESA ESTEC, Keplerlaan 1, PO Box 299, NL-2200 AG Noordwijk, The Netherlands, Email: Ugo.Lafont@esa.int*

ABSTRACT

Due to their self-repair ability and efficiency after high velocity impacts, ionomers can be used to protect future spacecraft from space debris. This work describes the characterization of the Ethylene-Methacrylic Acid (EMAA) based ionomer, potentially usable in space due to its excellent impact damage recovery properties.

Data from previous physical, impact and mechanical tests were used to better understand the EMAA ionomer behaviour. Among them, ballistic tests with different sample thicknesses and bullet speeds in the 1.9-4.1 km/s hypervelocity range were considered to assess the self-healing performance of this ionomer. Experimental results showed effective healing behaviour of the ionomer, suggesting it as a promising candidate for self-repairing space structures applications.

A numerical model was subsequently defined and proved to be suitable for preliminary simulation of the EMAA self-healing behaviour under hypervelocity impacts. Nevertheless, additional characterization is required to better reproduce the whole healing process.

1 INTRODUCTION

Self-healing polymers are gaining visibility in the field of space applications, as their ability to autonomously recover from damages might lead to innovative long-lasting space structures, way safer than current solutions.

In particular, a subset of thermoplastic polymers called ionomers can self-repair after puncture [1–3]. As an example, when a bullet impacts with an ionomeric panel, under certain geometrical and velocity conditions the energy transferred from the former to the latter is sufficiently high to cause viscoelasto-plastic deformation and heating of the material. This leads to the melting of the material in the impacted region, followed by cooling and possible local re-welding after the passage of the projectile, which might eventually close the hole created by the impact [4].

In-depth experimental analysis was conducted in previous studies to determine the effects of ionomer properties, damage characteristics and environmental conditions on self-healing performances [2], as well as the correlation between temperature variations and viscoelasticity of ionomers [4,5]. On the contrary, the development of analytical and numerical models for the description of the related self-healing process is still at an early stage. As a matter of fact, none of the constitutive equations currently exploited in the description of polymeric rheological-mechanical properties is able to fully account for the flow phenomena characterizing polymers [6]. Furthermore, numerical techniques typically used to simulate mechanical damage events are unable to satisfactorily reproduce the healing process [7].

The challenges in fully understanding the behaviour of self-healing ionomers are due to the several mechanisms involved in the process of reparation and related to very different time and rate scales [8–10]. In addition, as these materials undergo significant temperature variations when subjected to high velocity impacts, they can turn from solids to low viscosity fluids [3]. As a consequence, the assessment of material properties should either consider widely different experimental conditions or accept the introduction of approximations [11–13]. Having a suitable numerical model would instead improve the understanding of fast phenomena occurring in the material within few fractions of a second and could be used both in the selection of materials for given applications and in the determination of the related critical aspects.

This paper describes the characterization of an Ethylene-Methacrylic Acid (EMAA) based ionomer through the analysis of data from hypervelocity impact tests previously performed by Grande et al. in [4], followed by numerical modelling. Spherical projectiles and ionomer panels were used in the reference impact tests, and a constitutive law was then formulated to describe the material self-healing response to damage. The related model was then exploited to simulate two among the available hypervelocity tests and compare numerical and experimental results.

2 MATERIALS AND METHODS

2.1 Material

The material employed in the experimental work described in [4] is DuPont's Surlyn® 8940, a thermoplastic EMAA ionomer in which 30% of the

methacrylic acid (MAA) groups have been neutralized with sodium ions. It has a density of 0.95 g/cm^3 and a melting temperature of 94 °C.

Before manufacturing the samples, the material was dried under vacuum at 60 °C for five hours. 120x120 mm square plate specimens were then produced through compression moulding at 150 °C. Three different thicknesses of approximately 2 mm, 3 mm and 5 mm were considered.

Concerning the tensile tests, dog-bone specimens with 2 mm thickness were obtained following the ASTM D1708 standard.

2.2 Impact tests

In the here considered tests, conducted by Grande et al. [4], aluminium projectiles with a diameter $d = 1.5\ mm$ were shot at velocities between 1.9 km/s and 4.1 km/s, to simulate space conditions. The main purpose was to analyse the self-healing response of the ionomer after hypervelocity impacts reproducing collisions with micrometeoroids and orbital debris (MMOD). The performed tests and related information are listed in Tab. 1; parameter t in the last column indicates the sample thickness.

Table 1: Ballistic tests configurations [4].

Test	Bullet speed [km/s]	Sample thickness [mm]	t/d [-]
1	1.93	2	1.33
2	1.80	3	2.00
3	1.64	5	3.33
4	3.90	2	1.33
5	4.00	3	2.00
6	4.10	5	3.33

2.3 Tensile tests

Two types of uniaxial tensile tests were carried out in [4] to analyse the dependency of the stress-strain curves on both strain rate and temperature. The first set considered tests at 23 °C with crosshead speeds going from 0.1 to 500 mm/s, corresponding to strain rates from 4.5 x 10^{-3} to 22.7 s^{-1}. Temperature variations were also measured by means of an infrared camera.

On the other hand, temperature values from -40 to 60 °C were considered for the temperature-dependent experiments, and the employed crosshead speeds ranged from 10 to 500 mm/min, corresponding to strain rates between 7.5 x 10^{-3} to 3.8 x 10^{-1} s^{-1}.

2.4 Numerical model

The main innovative part of the here presented work is related to the creation of a novel material model for the analysed EMAA ionomer. An elasto-plastic model was considered which accounted for both temperature and strain rate variations. Concerning the elastic contribution, the material was assumed isotropic, hence needing only the Young's modulus E and the Poisson's ratio υ to be defined. Different values of E were taken from the 10 mm/min tensile tests at 23 °C, 40 °C and 60 °C to account for its dependence on temperature (Tab. 2), while υ was set to 0.4, a value related to polyethylene, which is comparable to the analysed EMAA ionomer [14]. Actually, υ typically varies with temperature and deformation rate, but it was here decided to keep it constant as a first approximation.

Table 2: Variation of the elastic modulus E with temperature T.

E [MPa]	T [K]
219.396	296
146.036	313
12.719	333

On the other hand, the Johnson-Cook model was chosen to describe plasticity, as this model accounts for strain rate dependency and is suitable for the representation of phenomena characterized by high strain rates and adiabatic transient dynamics. The related stress expression is:

$$\sigma = \left(A + B\varepsilon_{pl}{}^{n}\right)\left(1 + C\ln\frac{\dot{\varepsilon}}{\dot{\varepsilon}_0}\right)\left(1 - \hat{\theta}^{m}\right) \quad (1)$$

where ε_{pl} is the plastic deformation, $\dot{\varepsilon}$ is the strain rate, and $\hat{\theta}$ is a non-dimensional temperature defined as:

$$\begin{cases} 0 & if\ \theta < \theta_{trans} \\ \dfrac{\theta - \theta_{trans}}{\theta_{melt} - \theta_{trans}} & if\ \theta_{trans} \le \theta \le \theta_{melt} \\ 1 & if\ \theta \ge \theta_{melt} \end{cases} \quad (2)$$

$A, B, C, n, m, \theta_{trans}$ and θ_{melt} are the Johnson-Cook parameters to be calibrated, while $\dot{\varepsilon}_0$ is a reference strain rate.

In the initial calibration phase [15] a first set of values for the Johnson-Cook parameters was determined by setting the reference strain rate to 0.0076 s^{-1} (corresponding to 10 mm/min) and fitting the plastic part of the curves related to the following tensile tests [4]:

- quasi-static isothermal test at 23 °C and 10 mm/min (test 1)

- quasi-static isothermal test at 60 °C and 10 mm/min (test 2)
- dynamic isothermal test at 23 °C and 500 mm/s (test 3)

The plastic deformation, needed for the computation of the initial values, was determined for each curve:

$$\varepsilon_{pl} = \varepsilon - \frac{\sigma}{E} \qquad (3)$$

The elastic stress contribution was then removed to obtain plastic stress values σ_{pl}.

Parameter A was set equal to the true yield stress of test 1, which was also used for the computation of B and n through fitting of the curve with the expression $A + B{\varepsilon_{pl}}^n$ in Eq. 1. The chosen initial guess values were 5 MPa and 1 for B and n respectively.

θ_{trans} was set to 315 K, as this value was in the range of the real order-disorder transition temperature which affects the polymer. Test 2 was then used to determine m, because it was quasi-static and hence C was not present. The same curve fitting procedure used for determination of B and n was here exploited. In this case, the fitting expression was $\left(A + B{\varepsilon_{pl}}^n\right)\left(1 - \hat{\theta}^m\right)$, and an initial guess of 0.5 was used for m.

Finally, test 3 was exploited to determine C. Being an isothermal test, the contribution related to m was not present. In this case, the related expression was $\left(A + B{\varepsilon_{pl}}^n\right)\left(1 + C \ln\frac{\dot{\varepsilon}}{\dot{\varepsilon}_0}\right)$. The passages used for previous determination were here repeated with an initial guess of 0.5.

The resulting initial values of the Johnson-Cook parameters are listed in Tab. 3.

Table 3: Initial Johnson Cook parameters.

***A* [MPa]**	16.5237
***B* [MPa]**	38.7629
***n* [-]**	2.9348
***m* [-]**	0.3913
***C* [-]**	0.1367
θ_{trans} **[K]**	315
θ_{melt} **[K]**	367
$\dot{\varepsilon}_0$ **[s^{-1}]**	0.0076

Starting from these initial values, tensile tests were subsequently simulated with the Abaqus finite element analysis (FEA) tool to further tune the Johnson-Cook model. The specimen geometry was defined starting from the ASTM D1708 standard indications and its symmetry was exploited to reduce computational costs. Only half specimen was hence modelled (Fig. 1), and symmetry boundary conditions were applied to its central part. One of the specimen ends was then clamped, whereas a constant speed was imposed to the other one, corresponding to the strain rate of the selected test. After a preliminary mesh sensitivity study, a finer mesh was used for the central part of the specimen to improve the accuracy, and hexahedral elements were used to minimize mesh distortion.

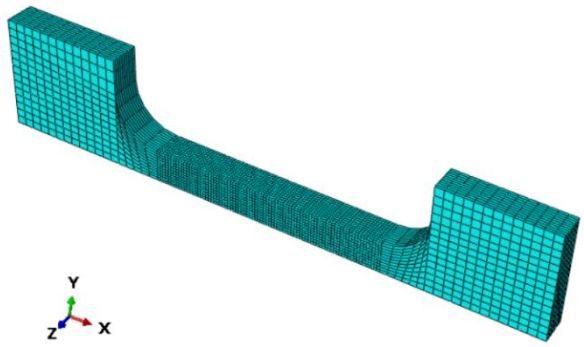

Figure 1: Half sample FEA model.

Failure was not modelled to avoid deletion of the elements meeting the related failure criterion, as the resulting lack of material would prevent satisfactory simulation of the complete self-healing process. The inelastic heat fraction was then set to 0.9 to simulate the plastic deformation contribution related to sample heating.

Different calibrations were made through comparison of experimental and simulated data and consequent adjustments of the Johnson-Cook parameters. The test at 500 mm/min and 23 °C was used to determine $n = 2.1$, which was then validated at the same temperature but with different strain rates of 10, 25, 65 and 180 mm/min. After that, the test at 40 °C and 10 mm/min was exploited to calibrate θ_{trans}. Finally, n was recalibrated by simulating the test at 23 °C and 500 mm/min and comparing it to experimental results. The ultimate Johnson-Cook parameters were used for further comparison with tests at 40 °C and 60 °C, again at 10 mm/min.

An equation of state (EOS) model was introduced in a second time, as it was useful for simulation of the impact tests. The Mie-Grüneisen model was chosen:

$$P - P_0 = \Gamma\rho\,(E - E_0) \qquad (5)$$

where P is the material pressure, E is the internal energy, ρ is the density, $\Gamma = \Gamma_0\rho_0/\rho$ is the Grüneisen parameter, and the 0 subscript indicates the reference state. A Hugoniot relation between the speed of the shock U_s and

the particle velocity U_p was also used to compute the state variables of the material:

$$U_s = c_0 + s \cdot U_p \quad (6)$$

The values of s and Γ_0 were set equal to the values typical of Ultra-High Molecular Weight Polyethylene [16], as this material is comparable to EMAA, and defined at 20 °C, close to the temperature at which the impact tests were performed. No calibration was performed in this case, but a test at 23 °C (E=219.396 MPa, v=0.4) and 500 mm/min was simulated to obtain the bulk speed of sound c_0:

$$c_0 = \sqrt{\frac{\lambda + 2\mu}{\rho}} \quad (7)$$

where λ and μ are the Lamé parameters, and $\rho = 950\ kg/m^3$ is the density of the material. The related EOS results were also compared with the Johnson-Cook fitting of the same curve.

2.5 Simulation of hypervelocity impacts

Hypervelocity impact tests 1 and 3 from [4] (Tab. 1) were simulated through the Abaqus FEA software, preferring a smoothed particle hydrodynamic (SPH) approach to the classical Eulerian one to avoid limitations related to the maximum number of mesh elements. It must be anyway pointed out that the SPH approach has high computational costs and times due to lengthy simulations and the required conversion of the mesh into particles.

Since it was experimentally observed that the impacts were not fully symmetric, the plates were modelled in their entirety without considering symmetry boundary conditions, imposing an encastre boundary condition on their edges. The projectiles were modelled as spherical rigid bodies, and they were constrained to move only along the direction perpendicular to the plate to simulate normal conditions related to the tests. Fig. 2 shows the FEA schematization of plate and projectile used for the simulations.

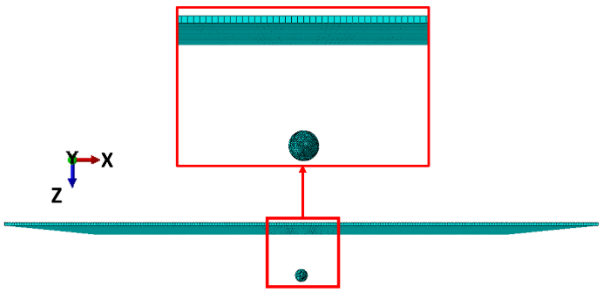

Figure 2: FEA plate and bullet models.

The plate was meshed with one element only along its thickness. The related SPH parameters are listed in Tab. 4. The initial temperature of the plate was set to 23 °C, as the ballistic tests were performed at room temperature.

Table 4: SPH parameters for impact simulations.

Test	Particles	Kernel
1	5	cubic
3	4	cubic

As impacts are characterized by large deformations and short duration, when simulating them it can be assumed that the volumetric and deviatoric responses of the material are separated. Isotropic shear elasticity was hence chosen to define the deviatoric stress-strain relationship:

$$S = 2\mu e^{el} \quad (4)$$

while the Mie-Grüneisen EOS formulation, previously defined in section 2.4, was used to describe the volumetric response.

General contact formulation with heat generation was then chosen to model contact between the plate and the projectile and account for dissipation of kinetic energy into heat. In these terms, a penalty formulation was used to model friction, setting the related coefficient to 0.3. Phase changes from solid to liquid state, and vice versa, were also modelled by introducing latent heat, solidus and liquidus temperature values [17] (Tab. 5).

Table 5: Latent heat model parameters [17].

Latent heat [J/kg]	$T_{solidus}$ [K]	$T_{liquidus}$ [K]
20800	296	367

3 RESULTS AND DISCUSSION

3.1 Impact tests

In the reference experimental study [4], Grande et al. noticed that all samples visually exhibited complete hole sealing in the case of bullet speeds close to 2 km/s, while at 4 km/s this was observed only in the 3- and 5-mm-thick samples (Tab. 6).

Morphological analysis following the impacts showed that all the tested plates had projectile fragments on their inlet side, which were on the other hand not detected at the exit side (Figs. from 6 to 9 in [4]).

The samples from tests 1, 4 and 5 indicated in Tab. 6 had similar morphologies of the damaged area (Figs. from 6

to 8 in [4]). The bullet entry zones showed an indented surface, while a meted area was clearly visible on the back of the samples, having a diameter comparable to the projectile in the case of test 1 (Fig. 6 in [4]) and of approximately 4 mm for tests 4 and 5 (Fig. 7 and Fig. 8 in [4]). Voids probably due to the generation of volatile substances during impacts were also detected. Sublimation led to significant and very rapid modification of the material properties.

The remaining samples were characterized by an impact crater with similar characteristics in the entry and exit sides. As shown in Fig. 3, in each side a melted zone was present alongside polymer filaments originating from the impacted area.

Due to the complexity of hypervelocity impacts, further tests and experimental characterization will need to be performed to fully understand the applicability of Surlyn® 8940 to self-healing space devices. Nevertheless, the material exhibits a promising behaviour.

Table 6:Hypervelocity impact tests results [4].

Test	Velocity [km/s]	Thickness [mm]	t/d [-]	Healing (hole closure)
1	1.93	2	1.33	Yes
2	1.80	3	2.00	Yes
3	1.64	5	3.33	Yes
4	3.90	2	1.33	No
5	4.00	3	2.00	Yes
6	4.10	5	3.33	Yes

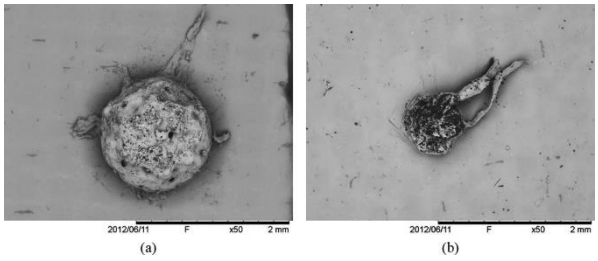

Figure 3: Test 2 sample entry (a) and exit (b) sides [4].

3.2 Tensile tests

The tensile curves obtained in [4] highlighted a strong dependence of the mechanical behaviour of Surlyn® 8940 on strain rate (Fig. 4). As a matter of fact, increasing the strain rate leads to higher values of the instantaneous Young's modulus and yield and post-yield stress. Nevertheless, it is also related to the decrease of strain at break.

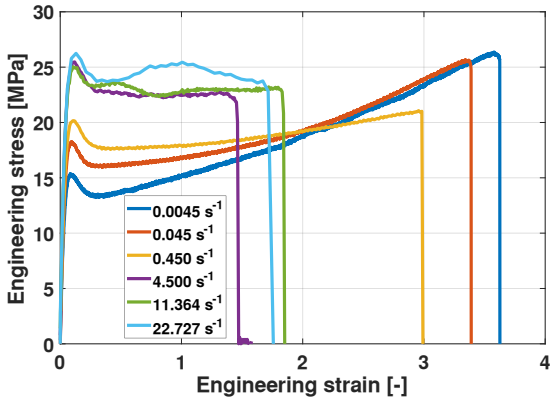

Figure 4: Stress vs. strain curves at different strain rates at 23 °C [4].

The specimens stretched at the highest strain rate were subjected to a temperature increase up to 32 °C due to deformation energy dissipation. All cases were characterised by significant plastic deformation with strain at break above 190%. Furthermore, infrared camera observations during the tests suggested homogeneity of temperature and plastic deformation in the samples. Nevertheless, it must be considered that temperatures are affected by heat exchange between the specimen and the environment.

Focusing on the stress-strain curves related to different initial specimen temperatures, it was observed that increasing the temperature up to 40 °C led to higher ultimate deformation and lower ultimate stress, reflecting a softening behaviour. In addition, the instantaneous Young's modulus and the yield stress decrease with increasing temperature. However, the increasing trend of the ultimate strain was arrested in the 60 °C curve, as clearly visible in Fig. 5. Furthermore, no significant peak yield stress was observed, as transitions due to melting of secondary crystals had already taken place and aging effects were absent.

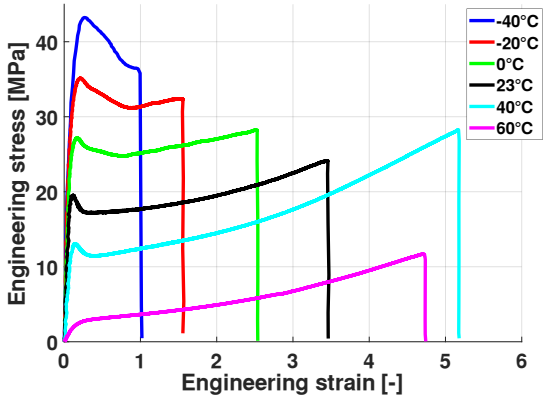

Figure 5: Stress vs. strain curves at different temperatures at 180 mm/min (0.136 s^{-1} strain rate) [4].

3.3 Material model

The final Johnson-Cook and Mie-Grüneisen parameters are listed in Tab. 7. Simulations run with the Johnson-Cook model and experimental results related to the tests at 23, 40 and 60 °C from [4] were compared for the 0.007.5 s^{-1} (10 mm/min) case (Fig. 6), and it was observed that the initial part of the curves was satisfactorily followed by the numerical model in all cases, while a marked difference appeared between experimental and simulated data in the final part of the curves. The m parameter might be decreased to partially overcome this issue.

Table 7: Calibrated material parameters.

A [MPa]	16.5237
B [MPa]	38.7692
n [-]	2.0875
m [-]	0.4835
C [-]	0.1367
θ_{trans} [K]	308
θ_{melt} [K]	367
$\dot{\varepsilon}_0$ [s^{-1}]	0.00776
s [-]	1.8
Γ_0 [-]	1.6
c_0 [m/s]	703.4755

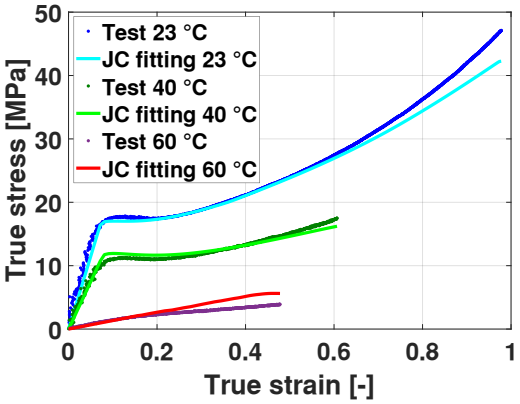

Figure 6: Experimental and simulated results at 0.0075 s^{-1} (10 mm/min).

A comparison was also made between the Johnson-Cook and the Mie-Grüneisen models for the test at 23 °C and 500 mm/min from [4], showing good accuracy and similarities in the results (Fig. 7).

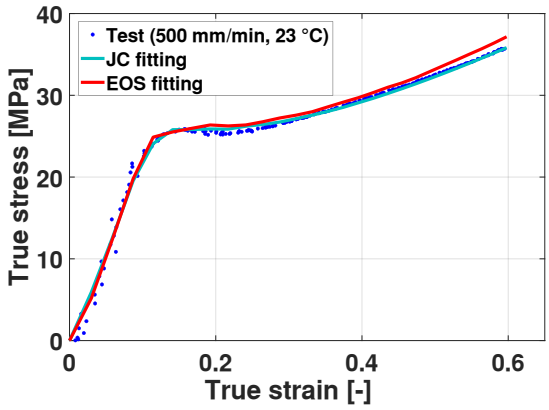

Figure 7: 500 mm/min test at 23 °C with Johnson-Cook and Mie-Grüneisen EOS fitting comparison.

One of the main limitations related to the Johnson-Cook model is given by the transition temperature θ_{trans}. As a matter of fact, the actual order-disorder transition temperature of Surlyn® 8940 spans from 23 °C to 42 °C and is related to a continuous change of the material properties [17,18]. This effect cannot be captured by the Johnson-Cook model because the definition of a single transition temperature value leads to neglection of thermal effects related to temperatures below the chosen θ_{trans}. Inserting an additional thermal parameter could hence help to better capture the material behaviour at different temperatures.

3.4 Hypervelocity impacts simulations

Simulations could only partially reproduce the self-healing process, which was started but not completed. This is indicated in Tab. 8, which also contains information about the obtained bullet exit velocity V_{out}.

Table 8: Hypervelocity impacts simulations results.

Test	**V_{out} [km/s]**	**Healing**
1	1.646	Started but not completed
3	0.477	Started but not completed

Fig. 8 and Fig. 9 show the comparison between simulated and experimental final impact conditions. As the outlet velocity was not experimentally measured, only visual comparison was performed.

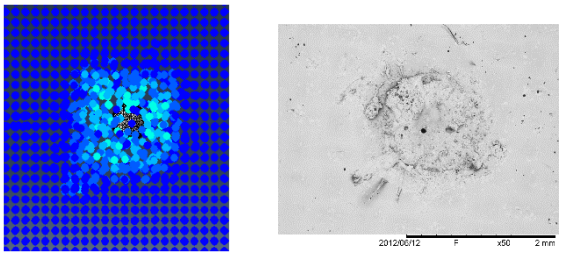

(a) (b)

Figure 8: Impact test 1 comparison between (a) simulated and (b) experimental results from [4].

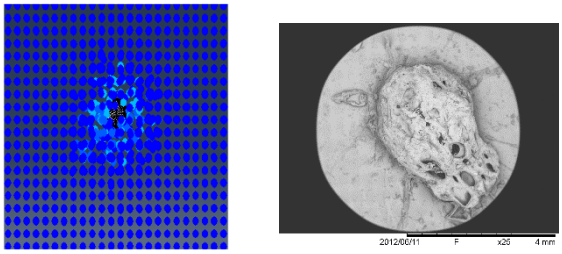

(a) (b)

Figure 9: Impact test 3 comparison between (a) simulated and (b) experimental results from [4].

As already said, in both simulations the beginning of the self-healing process is visible, but full hole closure is not reached due to the limits of the adopted model and assumptions. First of all, in the Johnson-Cook formulation the material does not offer any resistance once its temperature has exceeded the melting one, and sublimation, which is significant during impacts, is not modelled. Furthermore, neither strain rate dependence of the elastic modulus nor bullet deformation were modelled, while residues of the projectile were actually found in the impact areas, indicating bullet deformation and material loss.

4 CONCLUSIONS

After analysing the results of ballistic hypervelocity puncture tests and the mechanical properties of EMAA ionomer Surlyn® 8940 under different experimental conditions described in [4], the related data were used to calibrate the proposed elasto-plastic material model which was then exploited to simulate impact tests.

Ballistic tests were carried out firing spherical bullets at different speeds ranging approximately from 2 to 4 km/s and proved the ability of the material to self-heal under severe hypervelocity conditions, suggesting a possible use of the EMAA based ionomer in the space field.

Tensile tests and temperature recordings showed how the heat generated by plastic deformation seems to significantly contribute to the sealing of the hole after high energy impacts and underlined the strong dependence of the mechanical properties of the material on both temperature and strain rate.

From the subsequent model calibration and impact tests simulations, it was observed that the Johnson-Cook plasticity formulation cannot fully describe the self-healing behaviour. According to this model, the material does not offer any resistance once its temperature has exceeded the melting point, which is actually in contrast with the real behaviour of the analysed ionomer. As a matter of fact, even if the material is melted its viscous properties are still present and cannot be neglected due to phenomena like the ion hopping. More exhaustive and accurate results would be obtained, for example, through a visco-elasto-plastic model. The dependence of the elastic modulus not only on temperature, but also on the strain rate, should also be considered.

5 ACKNOWLEDGEMENTS

This research has been supported by ESA, contract No. 4000132669/20/NL/MH/ic.

6 REFERENCES

1. Pestka, K.A., Kalista, S.J., and Ricci, A. (2013) A proof of principle experiment: Structural transitions in self-healing poly (ethylene co-methacrylic acid) ionomers using acoustic and ultrasonic time dependent resonant spectroscopy. *AIP Adv.*, **3** (8).

2. Kalista Jr, Stephen J., Thomas C. Ward, and Z.O. (2007) Self-healing of poly (ethylene-co-methacrylic acid) copolymers following projectile puncture. *Mech. Adv. Mater. Struct.*, **4** (15), 391–397.

3. Kalista, S.J., and Ward, T.C. (2007) Thermal characteristics of the self-healing response in poly(ethylene-co-methacrylic acid) copolymers. *J. R. Soc. Interface*, **4** (13), 405–411.

4. Grande, A.M., Castelnovo, L., Landro, L. Di, Giacomuzzo, C., Francesconi, A., and Rahman, M.A. (2013) Rate-dependent self-healing behavior of an ethylene-co-methacrylic acid ionomer under high-energy impact conditions. *J. Appl. Polym. Sci.*, **130** (3), 1949–1958.

5. Grande, A.M., Coppi, S., Di Landro, L., Sala, G., Giacomuzzo, C., Francesconi, A., and Rahman, M.A. (2012) An experimental study of the self-healing behavior of ionomeric systems under ballistic impact tests. *Behav. Mech. Multifunct. Mater. Compos. 2012*, **8342** (November 2016), 83420U.

6. Tadmor, Zehev, and C.G.G. (2013) Principles of polymer processing 2013. *John Wiley Sons*.

7. Wu, D.Y., Meure, S., and Solomon, D. (2008) Self-healing polymeric materials: A review of

recent developments. *Prog. Polym. Sci.*, **33** (5), 479–522.

8. Barbero, E.J., Greco, F., and Lonetti, P. (2005) Continuum Damage-Healing Mechanics with application to self-healing composites. *Int. J. Damage Mech.*, **14** (1), 51–81.

9. Privman, V., Dementsov, A., and Sokolov, I. (2007) Modeling of self-healing polymer composites reinforced with nanoporous glass fibers. *J. Comput. Theor. Nanosci.*, **4** (1), 190–193.

10. Maiti, S., Shankar, C., Geubelle, P.H., and Kieffer, J. (2006) Continuum and molecular-level modeling of fatigue crack retardation in self-healing polymers. *J. Eng. Mater. Technol. Trans. ASME*, **128** (4), 595–602.

11. Zeng, X.S., Takahashi, M., Yamane, H., and Masuda, T. (1999) Stress relaxation under large step strain for ionomers based on ethylene-co-methacrylic acid copolymer in the melt state. *Nihon Reoroji Gakkaishi*, **27** (1), 59–62.

12. Zeng, X., Yamane, H., Takahashi, M., and Masuda, T. (1999) Structure And Properties Of Ionomers Based On Ethylene-Co-Methacrylic Acid Copolymer (Emaa) Effects Of Thermal History. *Zair. Soc. Mater. Sci. Japan*, **48**, 33–37.

13. Zeng, X., Takahashi, M., Yamane, H., Takigawa, T., and Masuda, T. (1999) Dynamic viscoelasticity of ionomers based on ethylene-co-methacrylic acid copolymer in the melt state. *Nihon Reoroji Gakkaishi*, **27** (1), 53–57.

14. Sahputra, I.H., and Echtermeyer, A.T. (2013) Effects of temperature and strain rate on the deformation of amorphous polyethylene: A comparison between molecular dynamics simulations and experimental results. *Model. Simul. Mater. Sci. Eng.*, **21** (6).

15. Jutras, M. (2008) Improvement of the characterisation method of the Johnson-Cook model.

16. Nguyen, L.H., Lässig, T.R., Ryan, S., Riedel, W., Mouritz, A.P., and Orifici, A.C. (2015) Numerical modelling of ultra-high molecular weight polyethylene composite under impact loading. *Procedia Eng.*, **103**, 436–443.

17. Grande, A.M. (2014) Self-healing ionomer based systems for aerospace applications.

18. Coppi, S. (2011) Analisi sperimentale del comportamento di un polimero autoriparante e sviluppo preliminare di un modello viscoelastico.